Materials Advances

ROYAL SOCIETY OF CHEMISTRY

PAPER

View Article Online
View Journal | View Issue

Cite this: *Mater. Adv.*, 2024, 5, 9809

A novel synthesis of inorganic–organic nanohybrid based on $SiW_{11}Co$@Cu–BTC/MWCNTs-COOH for electrocatalytic oxidation of dopamine†

Zahra Sadeghi and Somayeh Dianat *

Received 18th September 2024,
Accepted 14th November 2024

DOI: 10.1039/d4ma00940a

rsc.li/materials-advances

Polyoxometalate (POM)-based inorganic–organic hybrid compounds exhibit a remarkable range of properties. These compounds are distinguished by their strong acidity, oxygen-rich surfaces, and excellent redox capabilities. Importantly, they do not share the typical limitations of POMs, such as low specific surface area and instability in aqueous solutions. In this paper, we present the design of a novel modified glassy carbon electrode (GCE) using a tri-component nanocomposite consisting of $SiW_{11}O_{39}Co(H_2O)$ ($SiW_{11}Co$), Cu–BTC (BTC is benzene-1,3,5-tricarboxylate), and carboxyl functionalized multi-walled carbon nanotubes (MWCNTs-COOH) fabricated through a drop-casting method followed by electrodeposition reduction. The resulting hybrid nanocomposite ($SiW_{11}Co$@Cu–BTC/MWCNTs-COOH) was characterized using Fourier transform infrared spectroscopy (FT-IR), X-ray diffraction (XRD), and transmission electron microscopy (TEM). Additionally, elemental composition was analyzed *via* inductively coupled plasma-optical emission spectrometry (ICP-OES), while surface area and pore volume distribution were measured using Brunauer–Emmett–Teller (BET) analysis. The morphology, electrochemical properties, and electrocatalytic activity of the $SiW_{11}Co$@Cu–BTC/MWCNTs-COOH/GCE were evaluated through field emission scanning electron microscopy/energy-dispersive X-ray analysis (FE-SEM/EDX), voltammetry, and amperometry techniques. Under optimized conditions, the sensor exhibited outstanding electrocatalytic activity toward dopamine (DA), achieving two linear detection ranges of 5–80 μM and 80–600 μM, with a limit of detection (LOD) of 2.35 μM (S/N = 3) using square wave voltammetry (SWV). Furthermore, the sensor exhibited high repeatability and reproducibility, ensuring consistent performance across multiple measurements. It also showed robust stability and outstanding selectivity. The sensor's analytical performance was further validated by its successful application to real samples.

1. Introduction

Polyoxometalates (POMs) are a big family of polynuclear metal–oxygen clusters formed by d^0 transition-metals (*e.g.*, V^{5+}, Nb^{5+}, Ta^{5+}, Mo^{6+}, and W^{6+}).[1,2] POMs, especially Keggin POMs, because of their structural diversity, electronic features, and excellent redox character have applications in the different fields of catalysis,[3] optics,[4] electromagnetism,[5] biological science,[6,7] energy storage,[8,9] separation,[10,11] and electrochemistry.[12–15] One of the intriguing characteristics of POMs is their ability for anionic clusters to execute rapid, reversible, and sequential multi-electron transfer processes while preserving their structural integrity.[16,17] This property makes them desirable in electrocatalysis studies and electrochemical sensing. Despite these advantages, POMs remain encumbered by inherent challenges such as low specific surface area (SSA below 10 m^2 g^{-1}) and elevated solubility in aqueous solutions, which limit their suitability as electrocatalysts within chemically modified electrodes (CMEs).[18] Encapsulating or loading POMs onto porous materials or non-porous supports with a significant SSA can significantly mitigate issues such as leaching and aggregation. This approach enhances the electrochemical properties and electrocatalytic activities of POMs, thereby improving their overall performance.[18]

Over the past several decades, an increasing number of micro and nano-porous materials have emerged as viable supports for POMs, particularly in the form of carbon-based substances,[18,19] silica,[20] conducting polymers,[21] and metal–organic frameworks (MOFs).[2,15,22] Recently, MOFs have been the spotlight of porous materials in wide research areas, particularly in materials science and the chemical industry, due to their fantastic nature and unique properties. MOFs are

---

Department of Chemistry, Faculty of Sciences, University of Hormozgan, Bandar Abbas 79161-93145, Iran. E-mail: s.dianat@hormozgan.ac.ir

† Electronic supplementary information (ESI) available. See DOI: **https://doi.org/10.1039/d4ma00940a**

highly crystalline subsets of nanoporous materials consisting of metal nodes and multidentate organic ligands (as linkers) linked together through covalent bonds to fabricate infinite hollow structures.[23] The ability to choose a wide variety of metals and linkers in the preparation of MOFs can create adjustable structures with controllable nanopores that make unique properties such as ultra-high SSA, accessible metal sites, open framework structures, and designable functionalities in the obtained structures. Such unique properties can make these compounds promising candidates for application in different areas, like gas storage and separation,[24] drug delivery,[25,26] proton conduction,[27,28] solar cells,[29,30] supercapacitors,[31,32] biomedicine,[33,34] and especially catalysis,[35–37] and electrocatalysis.[38,39] Moreover, MOFs are recognized for their exceptional hosting properties due to their high internal SSA, long-range ordered structure, and the ability to fine-tune pore size and channel geometry, which contributes to their versatility in various applications.[18] Up to now, a variety of functional materials as guest molecules such as metal nanoparticles, quantum dots, metal oxides, enzymes, POMs, silica, and polymers have been effectively integrated with MOFs to produce MOF hybrid materials.[40] In MOF hybrid materials, the properties of both MOFs (porous structure, chemical versatility, and structural design capability) and guest molecules (catalytic, optical, electrical, magnetic activities, and mechanical strength) can be efficiently combined.[40] Additionally, the synergistic interaction between the d–π orbitals of POM clusters and the delocalized p–π electrons of a MOF can lead to the emergence of new physical and chemical properties.[41] MOF-199 (Cu–BTC) with the chemical formula of $[Cu_3(BTC)_2(H_2O)_3]_n$ (BTC is benzene-1,3,5-tricarboxylate) is one rigid MOF, that can be simply produced.[42] It has a 3D framework with open metal sites and suitable SSA (1660 $m^2\ g^{-1}$) and significant pore volume (0.69 $cm^3\ g^{-1}$) that allows the chemical functionalization of the channel inside layer.[41] Cu–BTC was synthesized for the first time in 1999 by Chui *et al.*[43] As stated by them, Cu–BTC has a 3D channel structure with a developed porous network (about 1 nm pore size). In fact, Cu^{2+} is the central cation and BTC constitutes the linker. The Cu–BTC with excellent electrochemical and electrocatalytic properties have been applied in electrochemical sensors to determine glucose,[44] nitrite,[45] ascorbic acid,[46] hydrazine,[47] H_2O_2,[48] ethanol,[49] NADH,[50] *etc.* The porous Cu–BTC can allow electrolyte or analytes to enter the channels while its porous structure is quite well retained.[44] However, there are limited studies that reported its performance in the electrochemical sensors. Ji *et al.*[51] developed a Cu–BTC modified carbon paste electrode (CPE) as a novel sensing platform for sunset yellow and tartrazine at the linearity range of 0.3 to 50 nM and 1.0 to 100 nM with a limit of detection (LOD) of 0.05, and 0.14 nM, respectively. Song *et al.*[44] developed a GOD/AuNPs/Cu–BTC MOFs/3D-KSCs electrode (GOD: glucose oxidase; AuNPs: gold nanoparticles; KSCs: macroporous carbon) for glucose detection with an excellent linearity range of 44.9 μM to 4.0 mM and 4.0 to 19 mM, and the LOD of 14.77 μM. Cao *et al.*[52] fabricated an electrochemical sensor based on a hierarchical Cu–BTC MOF material (Cu–BTC/ITO) for glyphosate detection. This Cu–BTC-based sensor displays a wide linearity range of 1.0×10^{-3} to 1.0 nM and 1.0 to 1.0×10^4 nM and LOD of 1.4×10^{-4} nM.

POM@M–BTC materials demonstrate exceptional electrochemical performance in sensing applications. Despite their promising attributes, there remains a need for further exploration into the electrochemical potential of these materials beyond their conventional applications.

Li *et al.*[53] have identified a POM-based NENU-5 composited with ketjenblack (KB) as a high performance electrochemical sensor for hydrogen peroxide (H_2O_2) detection. The composite catalyst has an excellent electrochemical detection efficiency, including a low LOD (1.03 μM), a broad linearity range (10 μM to 50 mM), and a high sensitivity (33.77 μA mM^{-1}), and also excellent stability and selectivity.

Zhang *et al.*[54] applied a one-step solvothermal approach to synthesize immobilized POM/Cu–BTC on carbon cloth (NENU-3/CC and NENU-5/CC). The homogeneous distribution of the POM/Cu–BTC across the conductive substrate enhances the stability and efficiency of electrocatalytic activity. The NENU-3/CC and NENU-5/CC demonstrated high electro-reduction of bromate under acidic conditions. Notably, NENU-3/CC achieved a sensitivity of 45.11 μA cm^{-2} mM^{-1} with a detection limit of 0.55 μM, whereas NENU-5/CC reached a sensitivity of 18.83 μA cm^{-2} mM^{-1} and a detection limit of 1.18 μM. Moreover, the results indicate that the two film electrodes exhibit superior electrochemical stability and selectivity, positioning them as effective sensor materials for bromate detection.

Yu *et al.*[55] synthesized a $Ag_5BW_{12}O_{40}$@Ag–BTC multifunctional compound and then demonstrated its excellent sensing performance for H_2O_2 detection. The reported sensors herein exhibited a wide detection range, extending from 0.4 μM to 0.27 mM and a low detection limit of 0.19 μM. These sensors also demonstrated excellent selectivity and stability.

Xu *et al.*[56] prepared a $Co_3Mo_7O_{24}$@Ag–BTC hybrid compound and used it as a H_2O_2 sensor. $Co_3Mo_7O_{24}$@Ag–BTC exhibited a comprehensive set of analytical capabilities, featuring a broad detection range (1 μM to 0.43 mM), a low detection limit (0.33 μM), and an excellent selectivity. Its recovery ability was validated through its use in detecting H_2O_2 in blood serum. The recovery value of 98.41% represents its practical utility.

Additionally, the immobilization of POMs on carbon nanomaterials has been extensively documented, which has been shown to enhance the catalytic and electrocatalytic properties of these materials.

Over the past decade, carbon nanotubes (CNTs) have been leveraged to augment the electrochemical efficiency of CMEs because of their distinctive chemical and physical features.[12] These nanostructures serve as ideal support matrices for POM-based catalysts, offering benefits such as superior structural integrity, enhanced mechanical properties, and excellent electronic conduction.[12] CNTs are members of the fullerene structural family, which are involved in single-walled carbon nanotubes (SWCNTs) and multi-walled carbon nanotubes (MWCNTs).[57] MWCNTs are particularly appealing for use as electrocatalysts because of their significant internal SSA, high chemical and physical stability, extensive electrochemical window, and superior electrical conductivity.[12,58,59] Until now, no reports are available of POM@M–BTC/MWCNT nanocomposites.

In this study, an innovative approach to electrode modification was employed by constructing a novel glassy carbon electrode (GCE) that is composed of a tri-component inorganic–organic nanocomposite $SiW_{11}O_{39}Co(H_2O)$@Cu–BTC/MWCNTs-COOH ($SiW_{11}Co$@Cu–BTC/MWCNTs-COOH/GCE) by the drop-casting method followed by an electrodeposition procedure. The Cu–BTC is selected for increasing the SSA, active site, stability, and selectivity, and using MWCNTs-COOH as a conductive substrate to assist electron-transfer between $SiW_{11}Co$@Cu–BTC and the GCE surface. The modified GCE was then utilized as an electrochemical sensor for the quantitative determination of dopamine (DA) *via* electrochemical methods. This approach allowed for the evaluation of electrochemical behavior, selectivity, reproducibility, repeatability, and recovery in real biological samples, providing a comprehensive assessment of the sensor's performance.

2. Experiment

2.1. Materials

The $K_6[SiW_{11}O_{39}Co(H_2O)]\cdot nH_2O$ ($SiW_{11}Co$) and Cu–BTC were synthesized following previously established procedures.[60,61] Tungstosilicic acid ($H_4SiW_{12}O_{40}\cdot nH_2O$, HSiW), acetic acid (HAc), potassium carbonate (K_2CO_3), potassium acetate (KOAc), cobalt(II) acetate tetrahydrate ($Co(OAc)_2\cdot 4H_2O$), sodium perchlorate ($NaClO_4$), phosphoric acid (H_3PO_4), sulfuric acid (H_2SO_4), boric acid (H_3BO_3), potassium hexacyanoferrate ($K_3[Fe(CN)_6]$), and DA were of analytical grade. All reagents and materials were procured from reputable commercial suppliers, specifically Merck and Sigma, and employed without more purification. MWCNTs-COOH (SSA 200 $m^2\ g^{-1}$) were bought from Tecnan company, Spain. All solutions were made in deionized water (DI, 18 MΩ cm (25 °C), Milli Q, Millipore Inc.). Phosphate buffer saline (PBS) solution was prepared by dilution of a stock solution of 0.01 M H_3PO_4 and subsequent pH adjustment using a solution of 0.5 M NaOH. Britton–Robinson buffer (BRB) solution was made by mixing the H_3PO_4 (0.04 M), H_3BO_3 (0.04 M), and HAc (0.04 M) that is titrated by NaOH (0.2 M) to obtain the desired pH (pH 3–9). A dopadic ampoule (Caspian Tamin Pharmaceutical Co., Rasht, Iran) containing 200 mg/5 mL of DA was used as the DA source of the pharmaceutical sample. Human blood serum samples were collected from a volunteer in Hakiman medical diagnostic lab (Bandar Abbas, Iran).

2.2. Apparatus

FT-IR spectra were recorded in the range 4000–400 cm^{-1} by a Spectrum Two Spectrometer–PerkinElmer. The crystalline structures of $SiW_{11}Co$, $SiW_{11}Co$@Cu–BTC, Cu–BTC, MWCNTs-COOH, and $SiW_{11}Co$@Cu–BTC/MWCNTs were studied using X-ray diffraction (XRD) on a Panalytical X′PertPro X-ray diffractometer with a Cu Kα radiation source (λ = 1.5418 Å). A transmission electron microscope (TEM, Philips EM208S-100 kV, Netherlands) was used to examine the morphology of the $SiW_{11}Co$, Cu–BTC, $SiW_{11}Co$@Cu–BTC, and $SiW_{11}Co$@Cu–BTC/MWCNTs-COOH compounds. To estimate the percent of immobilized $SiW_{11}Co$@Cu–BTC on the surface of MWCNTs-COOH, the tungsten contents of the $SiW_{11}Co$@Cu–BTC/MWCNTs-COOH were detected using inductively coupled plasma-optical emission spectrometry (ICP-OES) on a PerkinElmer Optima 7300 DV, Waltham, MA, USA. Nitrogen adsorption–desorption analysis was carried out at 77 K on a BElSORP-Mini, Microtrac Bel Corp instrument. SSA and pore size distribution curves of the Cu–BTC, $SiW_{11}Co$@Cu–BTC, and $SiW_{11}Co$@Cu–BTC/MWCNTs-COOH were characterized by the Brunauer–Emmett–Teller (BET) method, and the Barrett–Joyner–Halenda (BJH) algorithm. The morphology and elemental analyses of the bare, and modified GCEs (Cu–BTC/GCE, and $SiW_{11}Co$@Cu–BTC/MWCNTs-COOH/GCE) were characterized with field emission scanning electron microscopy (FE-SEM, Zeiss-SIGMA VP model, Germany), coupled with energy dispersive X-ray spectrometry (EDX) and EDX-mapping, which provided detailed insights into the material's structural features and elemental composition.

The electrochemical experiments were done by an Autolab PGSTAT 302N instrument (Eco-Chemie, Netherlands). A GCE (GR-2S/N, Detect Company, Tehran, Iran, diameter 2.0 mm), a commercial Ag/AgCl/3 M KCl electrode (Metrohm, Switzerland) and a Pt rod (IV-EL/EB-2200, Ivium, Eindhoven, Netherlands) were applied as the working electrode, reference electrode, and counter electrodes, respectively. All measurements were recorded with the Autolab NOVA 2.1.5 software. Before the electrochemical analysis, the electrolyte was saturated with argon gas (99.999% purity) for 15 minutes and covered by the argon atmosphere throughout the analysis. Electrochemical impedance tests were performed on a potentiostat/galvanostat instrument (EIS, Ivium v11108 Eindhoven, Netherlands) in $[Fe(CN)_6]^{3-/4-}$ (0.5 mM) solution in 0.01 M PBS (pH 3) containing KCl (0.1 M) at a frequency range of 0.01–10^5 Hz. The electrochemical experiments were executed under controlled ambient temperature conditions.

2.3. Synthesis of $SiW_{11}Co$@Cu–BTC

$Cu(OAc)_2\cdot H_2O$ (0.2 g, 1 mmol) and $SiW_{11}Co$ (0.27 g, 0.092 mmol) in DI water (10 mL) were stirred for 20 minutes (solution A). The pH of solution A was carefully adjusted to 3.5 by 1 M HCl aqueous solution. H_3BTC (0.14 g, 0.67 mmol) was dissolved in 10 mL C_2H_5OH (solution B). Solution B was gradually added to solution A with continuous stirring at 25 °C. A blue precipitate appeared immediately. The obtained precipitate was filtered and washed with ethanol and DI water (1 : 1). After drying at 25 °C for 24 h, the crystalline material was obtained.

2.4. Synthesis of $SiW_{11}Co$@Cu–BTC/MWCNTs-COOH

A suspension of $SiW_{11}Co$@Cu–BTC (5 mg) and MWCNTs-COOH (5 mg) in DI water (5 ml) was ready. The prepared suspension was stirred at 45 °C for 1 h and subsequently sonicated for 5 minutes to achieve a homogenous dispersion of $SiW_{11}Co$@Cu–BTC/MWCNTs-COOH.

2.5. Preparation of $SiW_{11}Co$@Cu–BTC/MWCNTs-COOH/GCE

The procedure of electrode modification is shown in Scheme 1. Initially, 10 μL of a suspension of $SiW_{11}Co$@Cu–BTC/MWCNTs-COOH in DI

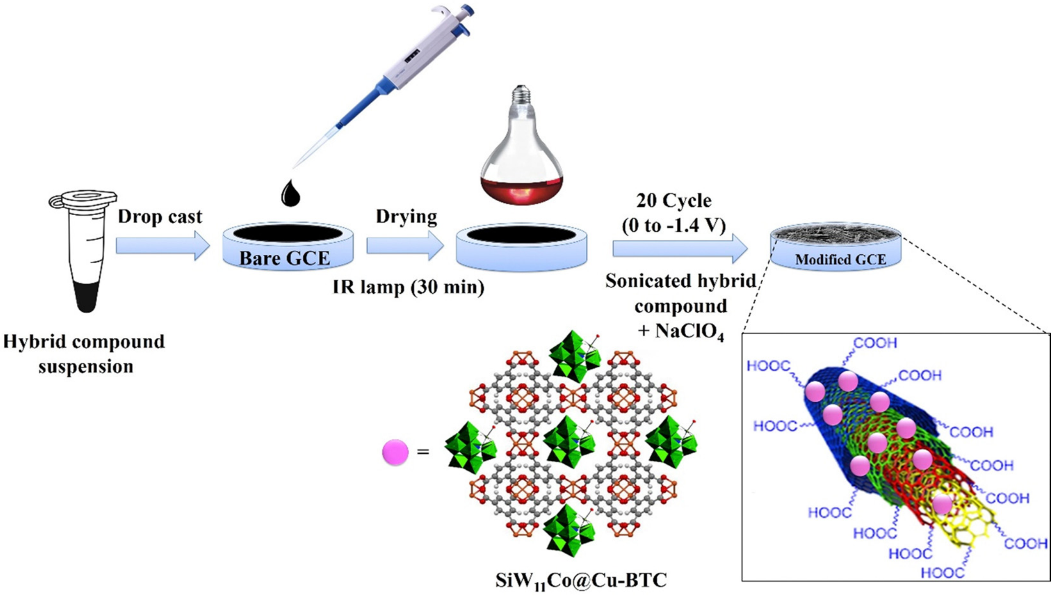

Scheme 1 Schematic diagram of the stepwise electrode modification processes.

water (1.0 mg mL^{-1}) was dropped on the bare GCE surface. Next, the GCE was dried by an IR lamp (250 W) for 30 minutes, and rinsed with DI water. Then, the GCE was subjected to twenty cycles within a defined potential range of 0 to −1.4 V with scan rate 25 mV s^{-1} in a sonicated suspension of SiW$_{11}$Co@Cu–BTC/MWCNTs-COOH (1.0 mg mL^{-1}) and NaClO$_4$ (0.2 M). The modified GCE was denoted as SiW$_{11}$Co@Cu–BTC/MWCNTs-COOH/GCE throughout the text.

3. Results and discussion

3.1. Characterizations of the nanohybrid compound

The loading percent of SiW$_{11}$Co over the MWCNTs-COOH surface was estimated to be 0.27% using ICP-OES spectroscopy. The FT-IR spectra of the SiW$_{11}$Co, SiW$_{11}$Co@Cu–BTC, Cu–BTC, MWCNTs-COOH, and SiW$_{11}$Co@Cu–BTC/MWCNTs-COOH are presented in the ESI† (Fig. S1). The detailed stretching

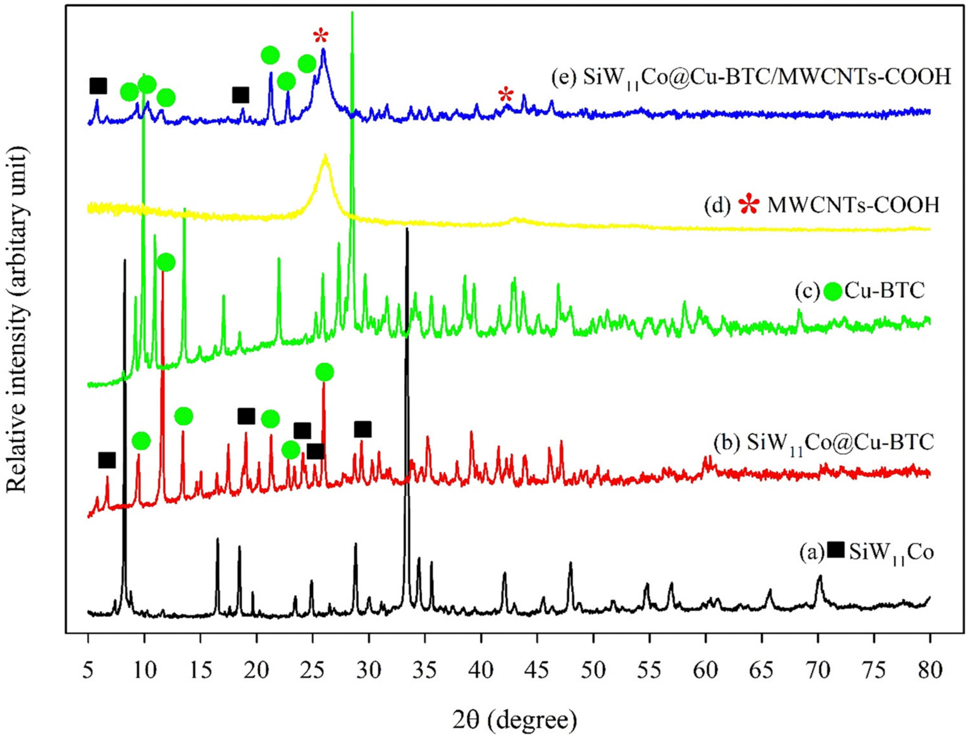

Fig. 1 XRD patterns of SiW$_{11}$Co (a), SiW$_{11}$Co@Cu–BTC (b), Cu–BTC (c), MWCNTs-COOH (d), and SiW$_{11}$Co@Cu–BTC/MWCNTs-COOH (e).

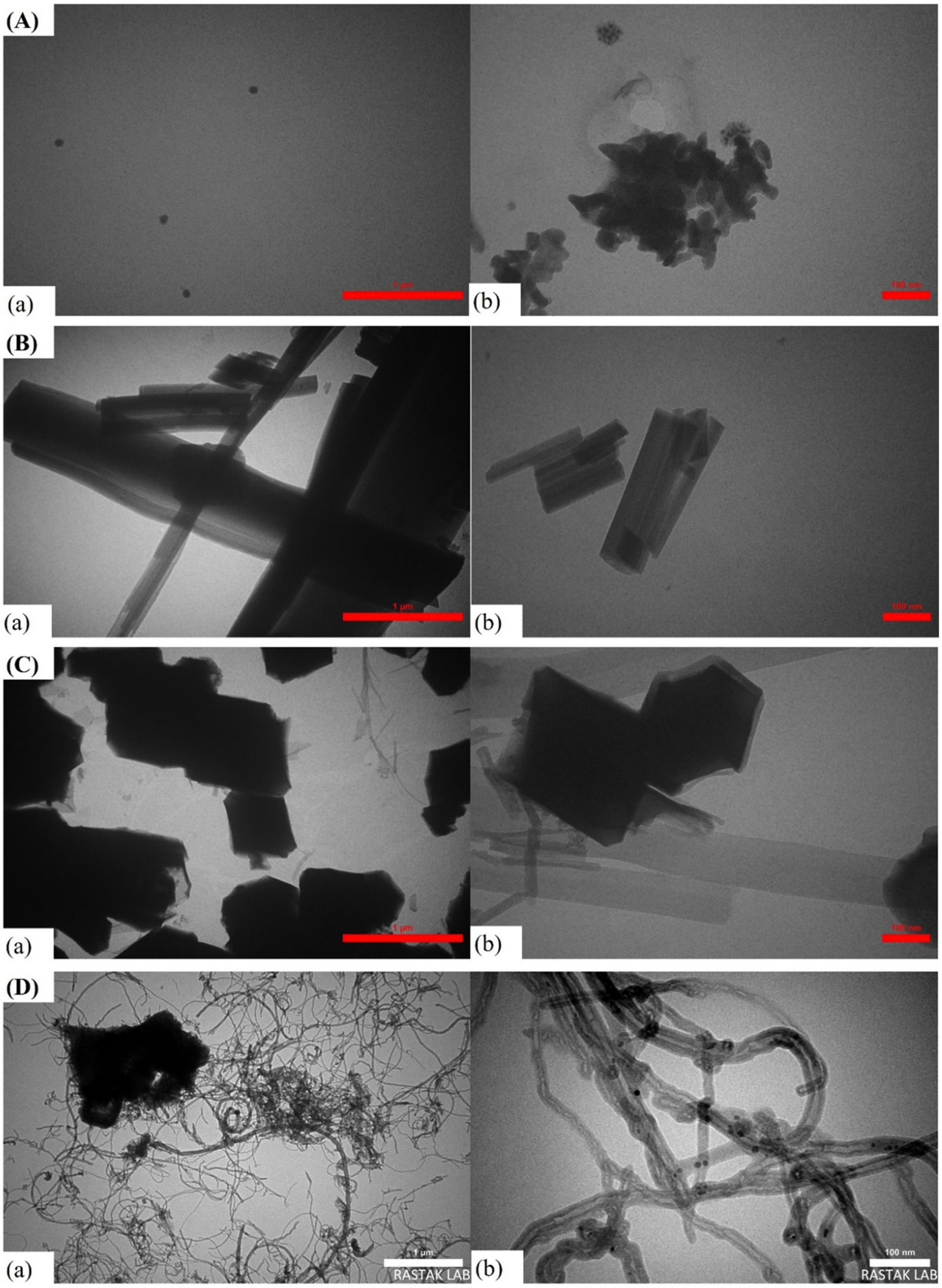

Fig. 2 TEM images of (A) $SiW_{11}Co$ (a) and (b), (B) Cu–BTC (a) and (b), (C) $SiW_{11}Co$@Cu–BTC (a) and (b), and (D) $SiW_{11}Co$@Cu–BTC/MWCNTs-COOH (a) and (b) at different magnifications.

frequencies ($\bar{\upsilon}$ cm^{-1}) assignments in the FT-IR spectra are given in Table S1 (ESI†). The obtained results of FT-IR confirmed that the $SiW_{11}Co$ by maintaining the Keggin structure was incorporated into the Cu–BTC cage, and also the $SiW_{11}Co$@Cu–BTC supported on the surface of MWCNTs-COOH.

The XRD patterns of $SiW_{11}Co$, $SiW_{11}Co$@Cu–BTC, Cu–BTC, MWCNTs-COOH, and $SiW_{11}Co$@Cu–BTC/MWCNTs-COOH are presented in Fig. 1. As displayed in Fig. 1b, $SiW_{11}Co$@Cu–BTC shows peaks at about 6.7°, and 19.1°, 24.2°, 25.2°, and 29.3°, which correspond to $SiW_{11}Co$ (Fig. 1a). However, peaks at about 9.4°, 11.6° 13.5°, 21.3°, 22.9°, and 25.9°, can be credited to the Cu–BTC (Fig. 1c). Fig. 1d shows two characteristic peaks at 25.9° and 42.3°, which correspond to (002) and (100) reflections of graphite from the MWCNTs-COOH, respectively. These results are consistent with the previous literature.[12] In Fig. 1e, the characteristic XRD peaks of $SiW_{11}Co$@Cu–BTC/MWCNTs-COOH appeared at nearly similar locations without a significant shift in its peak position compared to those of $SiW_{11}Co$, and Cu–BTC. This indicates that $SiW_{11}Co$ species in the $SiW_{11}Co$@Cu–BTC/MWCNTs-COOH hybrid nanocomposite still keep the Keggin structure. Furthermore, the presence of the characteristic peaks at 25.9° (002), and 42.3° (100) confirmed that

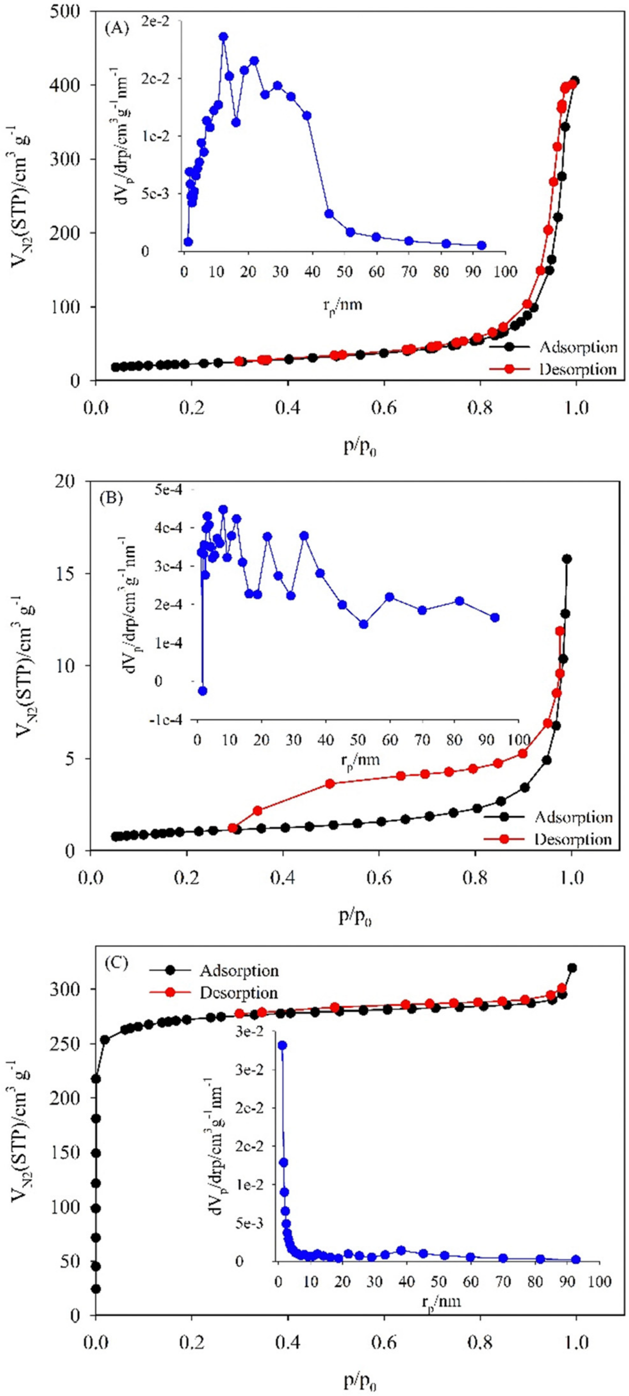

Fig. 3 Nitrogen adsorption–desorption BET isotherms of (A) Cu–BTC, (B) $SiW_{11}Co$@Cu–BTC, and (C) $SiW_{11}Co$@Cu–BTC/MWCNTs-COOH. The insets show the BJH-adsorption pore size distributions.

$SiW_{11}Co$@Cu–BTC was immobilized on the MWCNTs-COOH surface.

The morphology of $SiW_{11}Co$@Cu–BTC/MWCNTs-COOH was compared to $SiW_{11}Co$, Cu–BTC, and $SiW_{11}Co$@Cu–BTC at two magnification levels using TEM, as shown in Fig. 2. Fig. 2A displays $SiW_{11}Co$ which exhibits a spherical structure. Images a and b show that $SiW_{11}Co$ particles are dispersed, with some aggregation visible in image b, indicating that the particles are relatively small, scattered, and likely uniform in size distribution. Fig. 2B presents TEM images of Cu–BTC at two magnifications (images a and b), revealing elongated, rod-like crystals with a uniform shape, typical of MOF morphology. The rods are clearly resolved in image b, confirming the crystalline nature of the Cu–BTC. Fig. 2C shows the $SiW_{11}Co$@Cu–BTC composite (images a and b). The morphology changes from rod-like to hexagonal, suggesting that $SiW_{11}Co$ is well incorporated into the pores of Cu–BTC. At higher magnification (image b), distinct layers are visible, indicating strong interaction and integration between $SiW_{11}Co$ and Cu–BTC. Fig. 2D depicts the hybrid composite of $SiW_{11}Co$@Cu–BTC/MWCNTs-COOH. In image a, an entangled network of MWCNTs is evident, with $SiW_{11}Co$@Cu–BTC particles interspersed on the nanotube surface. Image b provides a closer view, showing a strong interaction between the nanotubes and nanocomposite particles, which could enhance the composite's stability and electrocatalytic activity.

Table 1 Textural and physicochemical properties of Cu–BTC, $SiW_{11}Co$@Cu–BTC, and $SiW_{11}Co$@Cu–BTC/MWCNTs-COOH

Sample	BET SSA (m^2 g^{-1})	Total pore volume (cm^3 g^{-1})	Mean pore diameter (nm)
Cu–BTC	81.1	0.6	28.9
$SiW_{11}Co$@Cu–BTC	3.7	0.02	25.4
$SiW_{11}Co$@Cu–BTC/MWCNTs-COOH	660.3	0.5	2.9

Fig. 3A–C shows the nitrogen adsorption–desorption isotherms of Cu–BTC, $SiW_{11}Co$@Cu–BTC, and $SiW_{11}Co$@Cu–BTC/MWCNTs-COOH. As shown in Fig. 3A and C, Cu–BTC and $SiW_{11}Co$@Cu–BTC/MWCNTs-COOH had type-III and type-I isotherms, respectively, which are characteristic of microporous materials. But the isotherm of the $SiW_{11}Co$@Cu–BTC material exhibits a type-IV isotherm, which is due to the ordered mesoporous structure in $SiW_{11}Co$@Cu–BTC. The isotherm of $SiW_{11}Co$@Cu–BTC displays a H4 hysteresis loop that is frequently linked with narrow slit-like pores (Fig. 3B). The pore size distribution diagrams (inset of Fig. 3A–C) show that most of the pore diameters of Cu–BTC, and $SiW_{11}Co$@Cu–BTC/MWCNTs-COOH are smaller than those of $SiW_{11}Co$@Cu–BTC, which confirms the microporous structure in Cu–BTC, and $SiW_{11}Co$@Cu–BTC/MWCNTs-COOH and mesoporous structure in $SiW_{11}Co$@Cu–BTC. Some textural properties of the synthesis samples are given in Table 1. As seen, the BET SSA, total pore volume, and mean pore diameter of $SiW_{11}Co$@Cu–BTC are sharply reduced compared to Cu–BTC, which should be credited to the occupation of pores of Cu–BTC by $SiW_{11}Co$ as guests. This phenomenon also indicates that $SiW_{11}Co$ is inserted into the pores of Cu–BTC rather than attached to the surface. However, the $SiW_{11}Co$@Cu–BTC/MWCNTs-COOH shows a considerable increase in BET SSA due to the immobilization of $SiW_{11}Co$@Cu–BTC on the surface of MWCNTs-COOH. It is believed that the more extensive BET SSA provides many active sites and more pathways for the diffusion of electrolyte ions, enhancing the electro-catalytic reaction.

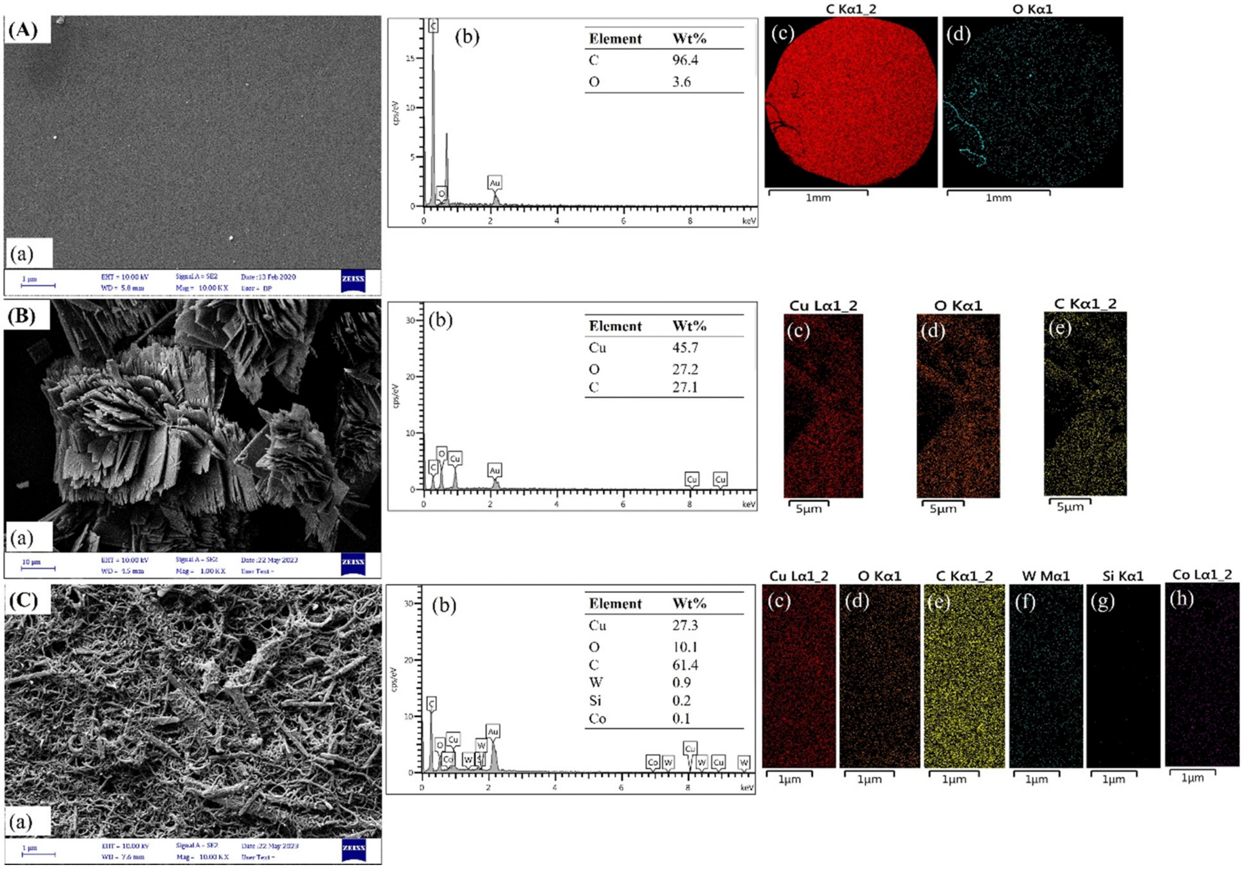

Fig. 4 FE-SEM images, EDX pattern, and EDX element mapping of the (A) bare GCE, (B) Cu–BTC/GCE, and (C) $SiW_{11}Co$@Cu–BTC/MWCNTs-COOH/GCE.

The morphology and chemical composition of the bare GCE, Cu–BTC/GCE, and $SiW_{11}Co$@Cu–BTC/MWCNTs-COOH/GCE were analyzed using FE-SEM/EDX. As shown in Fig. 4A, image a, the bare GCE has a mirror-like surface, which was reformed to a rough surface with modification by Cu–BTC, and SiW_{11}-Co@Cu–BTC/MWCNTs-COOH (Fig. 4B and C, image a). Furthermore, the EDX spectra of both bare and modified GCEs are depicted in Fig. 4A–C image b. The EDX patterns and elemental mappings confirm the presence of carbon (C) and oxygen (O) within the bare GCE (Fig. 4A, images b–d), Cu, O, and C in the Cu–BTC/GCE (Fig. 4B, images b–e) and Cu, O, C, W, Si, and Co elements on the $SiW_{11}Co$@Cu–BTC/MWCNTs-COOH/GCE (Fig. 4C, images b–h).

3.2. Electrochemical behavior of $SiW_{11}Co$@Cu–BTC/MWCNTs-COOH/GCE

The electrochemical behavior of the $SiW_{11}Co$@Cu–BTC/MWCNTs-COOH-modified GCE was investigated in 0.04 M BRB (pH 7) using CV, and the results were compared with those obtained from the bare GCE, $SiW_{11}Co$/GCE, Cu–BTC/GCE, and $SiW_{11}Co$@Cu–BTC/GCE. The results are shown in Fig. 5, which has been divided into three parts for better analysis.

Fig. 5A shows that the bare GCE exhibits no significant peaks. In contrast, the $SiW_{11}Co$/GCE displays two distinct cathodic peaks (I and II) at −0.35 V and −0.97 V, corresponding to the sequential electron transfer processes of $W^{6+} \rightarrow W^{5+} \rightarrow W^{4+}$. An anodic peak (I′) at −0.15 V, related to the $W^{5+} \rightarrow W^{6+}$ electron transfer, is also observed, with a ΔE_p of 0.20 V for the I/I′ redox couple.

Fig. 5B illustrates the electrochemical behavior of Cu–BTC/GCE, which shows two well-defined redox couples (I/I′ and II/II′) with ΔE_p values of 0.23 V and 0.25 V, respectively. These correspond to the sequential electron transfer processes of Cu^{2+}/Cu^{+} and Cu^{+}/Cu^{0}.

As shown in Fig. 5C, the $SiW_{11}Co$@Cu–BTC/GCE exhibits two cathodic peaks at −0.21 V (peak I) and −0.75 V (peak II), along with two anodic peaks at −0.04 V (peak I′) and −0.53 V (peak II′). These redox couples have lower ΔE_p values (0.17 V and 0.22 V for I/I′ and II/II′, respectively) compared to the Cu–BTC/GCE, indicating that the synergistic effect between $SiW_{11}Co$ and Cu–BTC facilitates electron transfer more efficiently.

For the $SiW_{11}Co$@Cu–BTC/MWCNTs-COOH/GCE (Fig. 5C), similar to $SiW_{11}Co$/GCE, two cathodic peaks (I, II) and an anodic peak (I′) are observed at more positive potentials: −0.21 V, −0.56 V, and 0.0 V for peaks I, II, and I′, respectively. i_p is lower than that of $SiW_{11}Co$/GCE but higher than that of Cu–BTC/GCE and $SiW_{11}Co$@Cu–BTC/GCE, which can be attributed to the presence of MWCNTs-COOH in the modified structure. The higher i_p suggests that MWCNTs-COOH acts as an efficient catalyst, enhancing electron transfer between the electrode surface and the $SiW_{11}Co$@Cu–BTC compound.

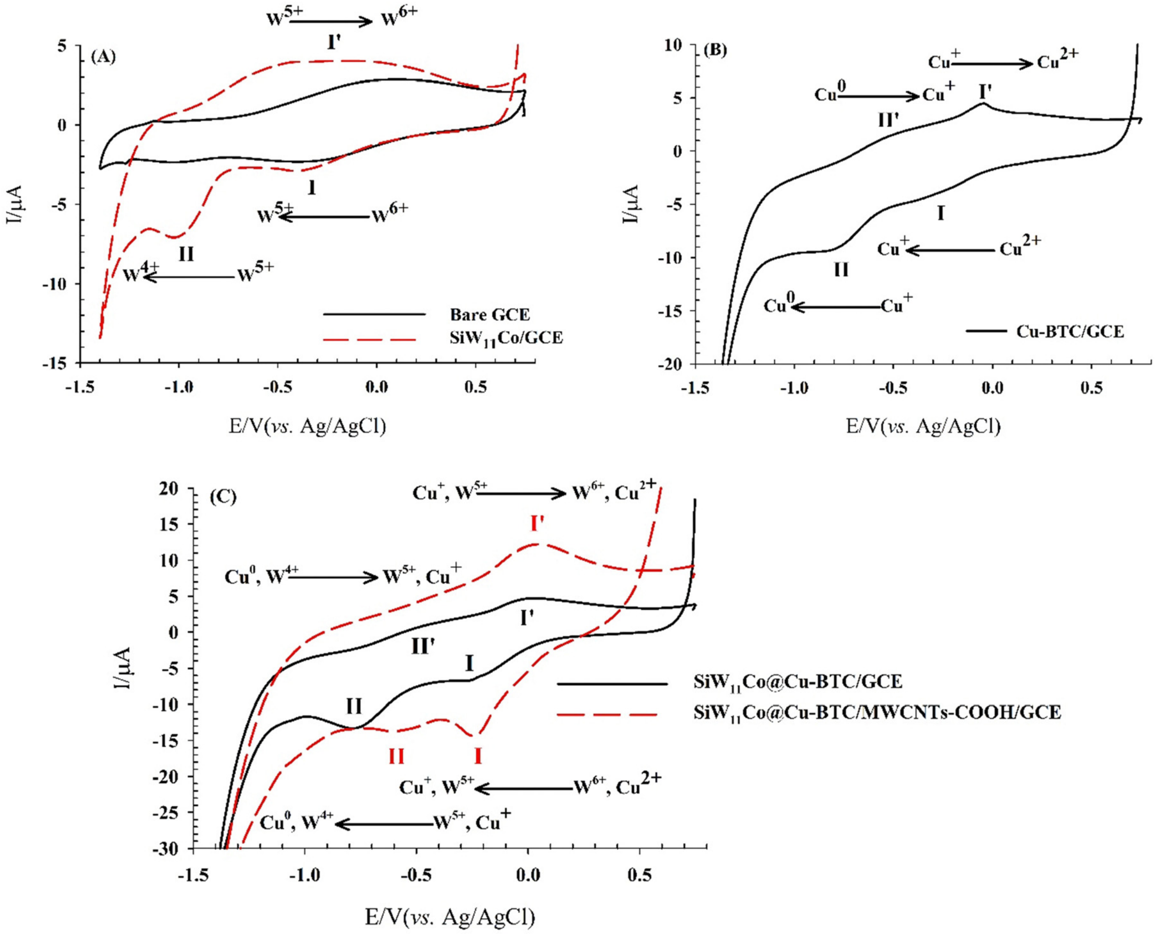

Fig. 5 CVs obtained on (A) bare GCE, and $SiW_{11}Co$/GCE, (B) Cu–BTC/GCE, and (C) $SiW_{11}Co$@Cu–BTC/GCE, and $SiW_{11}Co$@Cu–BTC/MWCNTs-COOH/GCE in 0.04 M BRB (pH 7) and scan rate of 50 mV s^{-1}.

Table 2 Electrochemical parameters extracted from CVs, for the I/I′ redox couple on the bare and modified GCEs in the presence of 0.5 mM $[Fe(CN)_6]^{3-/4-}$ in 0.01 M PBS (pH 3) containing 0.1 M KCl as supporting electrolyte

Electrode	ΔE_p/mV ± SD[a]	$\lvert i_{pc}\rvert$/μA ± SD[a]	i_{pa}/μA ± SD[a]
Bare GCE	70.81 ± 1.2	1.40 ± 0.18	1.44 ± 0.13
$SiW_{11}Co$/GCE	126.95 ± 1.1	0.96 ± 0.06	0.83 ± 0.08
$SiW_{11}Co$@Cu–BTC/GCE	87.89 ± 2.1	3.35 ± 0.17	3.86 ± 0.14
Cu–BTC/GCE	90.33 ± 0.9	2.73 ± 0.15	4.19 ± 0.12
MWCNTs-COOH/GCE	102.54 ± 1.1	4.38 ± 0.19	4.56 ± 0.17
$SiW_{11}Co$@Cu–BTC/MWCNTs-COOH/GCE	80.57 ± 1.4	23.82 ± 0.16	22.78 ± 0.18

[a] SD: Standard deviation (from 3 data point).

Given the proximity of the observed peak potentials for $SiW_{11}Co$@Cu–BTC/GCE and $SiW_{11}Co$@Cu–BTC/MWCNTs-COOH/GCE to the corresponding peaks in $SiW_{11}Co$/GCE and Cu–BTC/GCE, these peaks are likely associated with the sequential electron transfer processes of $W^{6+} \rightarrow W^{5+} \rightarrow W^{4+}$ and $Cu^{2+} \rightarrow Cu^{+} \rightarrow Cu^{0}$. The absence of the $W^{4+} \rightarrow W^{5+}$ and $Cu^{0} \rightarrow Cu^{+}$ electron transfer process in the $SiW_{11}Co$@Cu–BTC/MWCNTs-COOH/GCE is likely due to the high background current from the MWCNTs-COOH.

$[Fe(CN)_6]^{3-/4-}$ serves as a standard redox couple to assess the electron-transfer characteristics at the interface of the bare and different modified GCEs. Fig. S2-A (ESI†) illustrates that the bare GCE, $SiW_{11}Co$/GCE, and MWCNTs-COOH/GCE demonstrated a single redox couple (I/I′) corresponding to the Fe^{3+}/Fe^{2+} electron transfer. In contrast Cu–BTC/GCE, $SiW_{11}Co$@Cu–BTC/GCE, and $SiW_{11}Co$@Cu–BTC/MWCNTs-COOH/GCE exhibited two redox couples (I/I′ and II/II′). The I/I′ redox couple is likely associated with Fe^{3+}/Fe^{2+} and Cu^{2+}/Cu^{+} electron transfers, while the II/II′ couple is attributed to Cu^{+}/Cu^{0} electron transfers.[62] However, the peak current (i_p) and peak-to-peak potential separation (ΔE_p) for the I/I′ redox couple of the bare GCE were altered after modification. The electron-transfer kinetics of the $Fe(CN)_6^{3-/4-}$ redox couple at the surface of the modified GCEs is influenced by the electronic structure and thickness of the modifier layer.

As shown in Fig. S2-A (ESI†), the bare GCE exhibits a well-defined redox couple with a ΔE_p 70.81 mV, and i_{pc} 1.40 μA in 0.5 mM $Fe(CN)_6^{3-/4-}$ solution (pH 3) (curve a). However, a greater ΔE_p (126.95 mV) originates accompanied by decreasing i_{pc} (0.96 μA) at the $SiW_{11}Co$/GCE (Fig. S2-A, curve b, ESI†). The $SiW_{11}Co$ modifier acting as a protective barrier on the GCE effectively obstructs the electron-transfer process between the surface of the electrode and $[Fe(CN)_6]^{3-/4-}$ redox probe. The $SiW_{11}Co$@Cu–BTC/GCE (Fig. S2-A, curve c, ESI†) shows a smaller ΔE_p (87.89 mV) and more extensive i_{pc} (3.35 μA) than the $SiW_{11}Co$/GCE and Cu–BTC/GCE (Fig. S2-A, curves b and d, ESI†). The better electrochemical behavior of the $SiW_{11}Co$@Cu–BTC/GCE *versus* $SiW_{11}Co$, and Cu–BTC films can be credited to the synergistic interaction between the POM, and MOF blocks. As illustrated in Fig. S2-A, curve e (ESI†), the MWCNTs-COOH/GCE exhibits a substantial background current with more ΔE_p (102.54 mV) than the bare GCE. But with immobilizing the $SiW_{11}Co$@Cu–BTC on the MWCNTs-COOH substrate, ΔE_p decreases and i_p increases (Fig. S2-A, curve f, ESI†). Therefore, the $SiW_{11}Co$@Cu–BTC/MWCNTs-COOH/GCE demonstrates superior electrochemical performance due to the synergistic influence of the POM, MOF, and MWCNTs-COOH substrate. The extracted electrochemical parameters from these voltammograms for the I/I′ redox couple are tabulated in Table 2.

Moreover, EIS serves as a robust analytical tool for examining the interfacial properties of electrochemical sensors.[63] Fig. S2-B (ESI†) displays the Nyquist plots for the bare GCE, $SiW_{11}Co$/GCE, and $SiW_{11}Co$@Cu–BTC/MWCNTs-COOH/GCE. The bare GCE and $SiW_{11}Co$@Cu–BTC/MWCNTs-COOH/GCE did not exhibit any semi-circle in the Nyquist plot, likely due to the high electrical conductivity of these surfaces and the specific solution conditions. However, the charge-transfer resistance (R_{ct}) values for the bare and modified GCEs were calculated by fitting an equivalent electrical circuit. Upon modification with $SiW_{11}Co$, a semi-circle appeared in the Nyquist plot of $SiW_{11}Co$/GCE, and the R_{ct} value increased significantly from 780 Ω to 121 kΩ. This substantial increase is attributed to the low electrical conductivity of $SiW_{11}Co$ and the electrostatic repulsion between the negatively charged $SiW_{11}Co$ and the $[Fe(CN)_6]^{3-/4-}$ redox probe. Notably, after modification with $SiW_{11}Co$@Cu–BTC/MWCNTs-COOH, the R_{ct} decreased to 430 Ω. This decrease indicates the formation of a conductive adsorbed layer, which enhances electron transfer between the redox couple and the electrode surface. The reduced R_{ct} for $SiW_{11}Co$@Cu–BTC/MWCNTs-COOH/GCE compared to $SiW_{11}Co$/GCE can be attributed to the superior conductivity and electronic properties of the Cu–BTC and MWCNTs-COOH components.

3.3. Electro-active surface area of $SiW_{11}Co$@Cu–BTC/MWCNTs-COOH/GCE

The electro-active surface area of the $SiW_{11}Co$@Cu–BTC/MWCNTs-COOH/GCE was calculated and then compared with bare GCE, $SiW_{11}Co$/GCE, Cu–BTC/GCE, $SiW_{11}Co$@Cu–BTC/GCE, MWCNTs-COOH/GCE, and using the Randles–Sevcik equation (Eqn (1)) by the CV method in 0.5 mM $[Fe(CN)_6]^{3-/4-}$ solution in 0.01 M PBS (pH 3) containing 0.1 M KCl at various scan rates.[64,65] CVs were presented in the ESI,† Fig. S3 (ESI†).

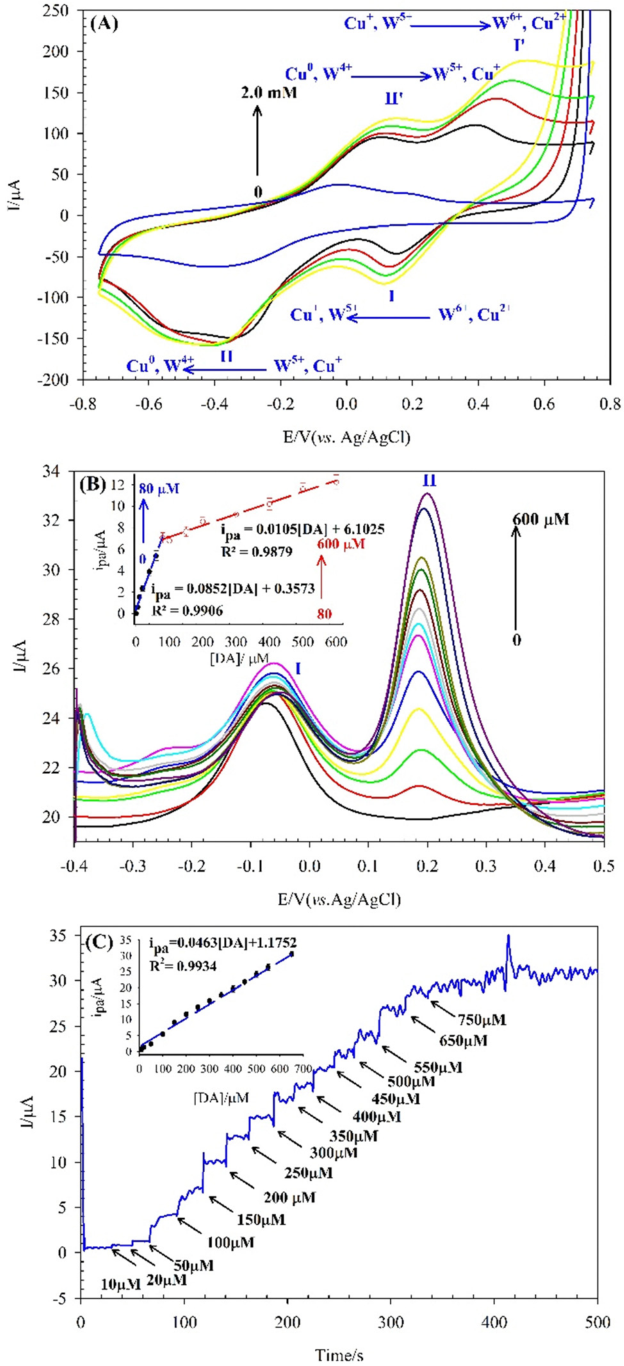

Fig. 6 Responses of $SiW_{11}Co$@Cu–BTC/MWCNTs-COOH/GCE for the determination of DA in 0.04 M BRB (pH 7) by (A) CV; scan rate 50 mV s^{-1}, dashed lines show shifts in peak potentials (B) SWV; step potential 1 mV, amplitude potential 20 mV. The inset shows a corresponding calibration plot of DA determination (peak II), and (C) chronoamperometry at the optimum potential of +0.25 V. The inset shows a corresponding calibration plot of the steady-state currents obtained against concentrations of DA.

Table 3 Comparison between the present study and other literature studies for the determination of DA

Modified electrode	Sweep mode	pH	E (V *vs.* Ag/AgCl)	linearity range (μM)	LOD (μM)	Ref.
Pt-CNT-GR[a]/GCE	DPV[b]	7.0	0.12	0.1–30	0.01	66
rGO/PAMAM[c]/MWCNT/AuNP[d]/GCE	DPV	4.0	0.36	10–320	3.33	67
Pd-NC[e]/rGO/GCE	*I–t*	7.4	0.25	20–220	7.02	68
$LiMnPO_4$/f-MWCNT/GCE	DPV	7.0	0.16	0.1–49	0.019	69
NA[f]/MWCNTs-β-CD[g]/GCE	DPV	7.0	0.14	0.01–1 1–10	0.005	70
GCE-ERGO/polyCoTAPc	DPV	7.4	0.012	2–100	0.095	71
$[P_2W_{17}V/CS]_6$/ITO-GCE	*I–t*	7.0	0.57	0.01–300	0.18	72
HKUST-1[h]/GCE	DPV	6.0	0.39	0.5–100	0.15	73
MOFs/ERGO-GCE	DPV	6.0	0.2	0.2–300	0.013	74
Fe-MOF/GCE	DPV	7.0	0.22	10–90	3.34	75
SiWCo/Cu–BTC/MWCNTs-COOH-GCE	SWV	7.0	0.20	5–80 80–600	2.35	Present study
	I–t		0.25	10–650	2.68	

[a] Graphene. [b] Differential pulse voltammetry. [c] Poly(amido-amine). [d] Au nanoparticle. [e] Palladium nanocube. [f] Nafion. [g] β-cyclodextrin. [h] $Cu_3(BTC)_2$.

$$i_p = 2.69 \times 10^5 n^{3/2} A_{\text{eff}} D_0{}^{1/2} \nu^{1/2} C_p \qquad (1)$$

where i_p (A) is the peak current (peak I′ here), n is the number of transferred electrons in the redox reaction (n = 1 here), A_{eff} (cm^2) is the electro-active surface area, D_0 (cm^2 s^{-1}) is the diffusion coefficient of $[Fe(CN)_6]^{3-/4-}$ (7.6 × 10^{-6} cm^2 s^{-1}), $\nu^{1/2}$ (V s^{-1})$^{1/2}$ is the square root of scan rate, and C_p (mol cm^{-3}) is the concentration of the probe solution (5.0 × 10^{-4} mol cm^{-3} here). The electro-active surface area of the $SiW_{11}Co$@Cu–BTC/MWCNTs-COOH/GCE was determined to be 92.65 cm^2, according to the linear equation of $i_{pa} = 34.3560\nu^{1/2} - 66.6530$ (R^2 = 0.9852) (Fig. S3-F, ESI†), which is approximately 150 times greater than that of the bare GCE (0.604 cm^2) with a linear equation of $i_{pa} = 0.2241\nu^{1/2} + 0.0435$ (R^2 = 0.9989) (Fig. S3-A, ESI†). Moreover, the electro-active surface area of the $SiW_{11}Co$@Cu–BTC/MWCNTs-COOH/GCE is higher than $SiW_{11}Co$/GCE (0.228 cm^2), Cu–BTC/GCE (0.766 cm^2), $SiW_{11}Co$@Cu–BTC/GCE (0.973 cm^2), and MWCNTs-COOH/GCE (1.66 cm^2) with linear equations of $i_{pa} = 0.0846\nu^{1/2} + 0.2891$ (R^2 = 0.9932), $i_{pa} = 0.2840\nu^{1/2} + 2.4952$ (R^2 = 0.9918), $i_{pa} = 0.3610\nu^{1/2} + 1.3600$ (R^2 = 0.9972), and $i_{pa} = 0.6177\nu^{1/2} - 0.2293$ (R^2 = 0.9835), respectively (Fig. S3-B–E, ESI†). This observation underscores the beneficial influence of MWCNTs-COOH on the electro-active surface area and overall electrochemical performance of the modified GCE.

3.4. Electrocatalytic properties of $SiW_{11}Co$@Cu–BTC/MWCNTs-COOH/GCE

Fig. 6A shows the CVs of the $SiW_{11}Co$@Cu–BTC/MWCNTs-COOH/GCE in 0.04 M BRB (pH 7) containing DA at different concentrations (0 to 2.0 mM) in the 0.75 to −0.75 V potential range. The findings reveal that the $SiW_{11}Co$@Cu–BTC/MWCNTs-COOH/GCE exhibits significant potential for DA detection, as evidenced by the progressive increase in two anodic peak currents (peaks I′ and II′) with rising DA concentrations. Peaks I′ and II′ correspond to two consecutive one-electron transfer processes of $W^{4+} \rightarrow W^{5+} \rightarrow W^{6+}$ along with $Cu^0 \rightarrow Cu^+ \rightarrow Cu^{2+}$ electron transfer processes. These electron transfers facilitate the oxidation of DA, confirming a reciprocal electrocatalytic interaction between the modifier and DA. Moreover, with the addition of DA, a new redox pair (I, I′ peak) appears, which demonstrates a reciprocal electrocatalytic interaction between the modifier and DA.

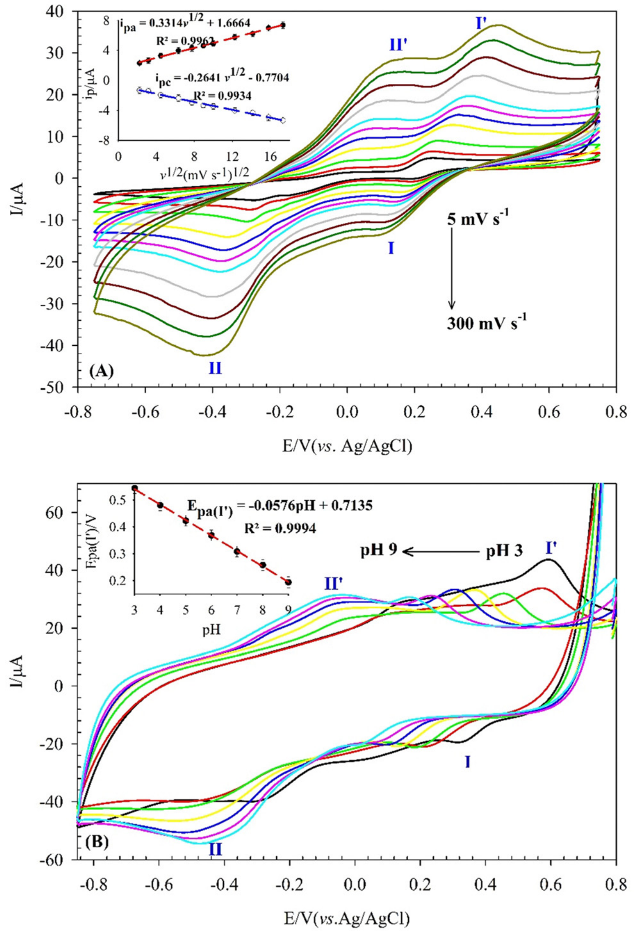

Fig. 7 (A) CVs of $SiW_{11}Co$@Cu–BTC/MWCNTs-COOH/GCE in 0.04 M BRB (pH 7) (A) in the presence of 0.5 mM DA at different scan rates from 5 to 300 mV s^{-1}. The inset shows variations of the anodic and cathodic peak currents (peaks I, I′) with scan rate. (B) In the presence of 200 μM DA at different pHs (pH 3–9); scan rate 50 mV s^{-1}. The inset shows the variation of the anodic peak potentials (E_{pa}) with pH.

However, the CV method, despite being a widely used technique for electrochemical analysis, is unable to satisfy the required conditions for quantitative analysis due to inherent limitations such as low sensitivity and high LOD. Utilizing square wave voltammetry (SWV) and chronoamperometry methods, which offer advantages such as low LOD and high sensitivity, ensured precise measurements for the DA sensing at the $SiW_{11}Co$@Cu–BTC/MWCNTs-COOH/GCE.

3.4.1. Voltammetric determination of DA. The responses of the SWV at the $SiW_{11}Co$@Cu–BTC/MWCNTs-COOH/GCE to DA in 0.04 M BRB (pH 7) are displayed in Fig. 6B. The calibration plot for the quantification of DA was established by graphing the correlation between peak II current and DA concentration under optimal experimental conditions, as depicted in the inset of Fig. 6B. The peak I did not show a regular response to DA. Therefore, it was not included in the quantitative measurements. The relative increase of the i_p (peak II) with the rise in DA concentration was demonstrated across two linear ranges of 5–80 μM and 80–600 μM with linear equations of i_p (μA) = 0.0852[DA] (μM) + 0.3573 (R^2 = 0.9906), and i_p (μA) = 0.0105[DA] (μM) + 6.1025 (R^2 = 0.9879) with LOD of 2.35 μM, LOQ of 7.84 μM, and sensitivity of 85.2 μA mM^{-1}. The LOD and LOQ were calculated using the equations LOD = $3S_b/m$ and LOQ = $10S_b/m$, where S_b represents the standard deviation of the twenty responses of the blank solution responses, and m is the slope of the regression line.

3.4.2. Amperometric determination of DA. Amperometric analysis was employed to evaluate the sensing capabilities of the $SiW_{11}Co$@Cu–BTC/MWCNTs-COOH/GCE in detecting DA, with corresponding data plotted in Fig. 6C. A rapid increase in current response was observed when DA was added to the 0.04 M BRB (pH 7) at an optimal potential of +0.25 V. This progressive increase in current with continued DA additions, indicates a highly effective electron-transfer rate of the modifier and the fast diffusion of DA from the electrolyte to the surface of the modified electrode. The calibration curve displayed in the inset of Fig. 6C indicated that $SiW_{11}Co$@Cu–BTC/MWCNTs-COOH/GCE shows a linear response range from 10 to 650 μM with a linear equation of i_{pa} (μA) = 0.0463[DA] (μM) + 1.1752 (R^2 = 0.9934), LOD of 2.68 μM, LOQ of 8.93 μM, and sensitivity of 46.3 μA mM^{-1}. However, at higher concentrations of 650 μM, the noise of the amperometric signal increases, and the current stabilization takes longer and longer until no straight line is achieved anymore.

In Table 3, a comparison is made between the LOD, linearity range values, pH and potential of the present sensor and other literature studies for the determination of DA. The tabulated results display that although the LOD of $SiW_{11}Co$@Cu–BTC/MWCNTs-COOH/GCE is slightly higher than some studies, it responds to DA in a wider linear range.

3.5. Electro-oxidation mechanism of DA

The mechanism of DA electro-oxidation at the $SiW_{11}Co$@Cu–BTC/MWCNTs-COOH/GCE was proposed by examining the effects of scan rate and pH on the i_p and E_p, respectively. Fig. 7A shows the CVs of 0.5 mM DA in 0.04 M BRB (pH 7) at the $SiW_{11}Co$@Cu–BTC/MWCNTs-COOH/GCE, recorded at various scan rates (5–300 mV s^{-1}). The anodic and cathodic peak currents (peaks I, I′) of DA exhibited a linear relationship with the square root of the scan rate ($\nu^{1/2}$) (inset of Fig. 7A). The linear regression equations for the anodic and cathodic peak currents were $i_{pa}(\mu A) = 0.3314\nu^{1/2}$ ($mV^{1/2}s^{-1/2}$) + 1.6664 (R^2 = 0.9962) and $i_{pc}(\mu A) = -0.2641\nu^{1/2}$ ($mV^{1/2}$ $s^{-1/2}$) − 0.7704 (R^2 = 0.9934), respectively. These results support the conclusion that the electro-oxidation of DA at the $SiW_{11}Co$@Cu–BTC/MWCNTs-COOH/GCE is a diffusion-controlled redox process, where the oxidation reaction is governed by the diffusion rate of DA from the electrolyte to the electrode surface.

The influence of pH on the E_{pa} of 200 μM DA was studied by the CV method over a pH range from 3 to 9 in a BRB solution, as depicted in Fig. 7B. The results show a progressive shift of the E_{pa} towards more negative values as the pH increased from 3 to 9. This finding confirms that DA oxidation at the $SiW_{11}Co$@Cu–BTC/MWCNTs-COOH/GCE involves a proton-mediated catalytic process.[76] A pronounced relationship was discerned between the E_{pa} and pH with the linear equation of E_{pa} (V) = −0.0576 pH + 0.7135 (R^2 = 0.9994) (inset of Fig. 7B). The obtained slope value of 57.6 mV pH^{-1} is near the theoretical value of 59.2 mV pH^{-1}. This confirms that the electro-oxidation of DA at the $SiW_{11}Co$@Cu–BTC/MWCNTs-COOH/GCE is balanced, with equal contributions from protons and electrons. Additionally, as shown in Fig. S4 (ESI†), both the POM and MOF components contribute to the electro-oxidation of DA. The proposed mechanism of DA electro-oxidation is shown in Scheme 2. For simplicity and clarity, only the relevant part of the modifier involved in the electron transfer is represented in the mechanism. Moreover, the oxidation states of W and Cu atoms are specified to provide a clearer illustration of the electron transfer process within the modifier. However, DA electrocatalytic oxidation at the nanohybrid-modified GCE can be explained as follows: the $[SiW_4{}^{V}W_7{}^{VI}Co@Cu_x{}^{I}Cu_y{}^{II}\text{–}BTC]$ portion of the modifier undergoes electro-oxidation to $[SiW_3{}^{V}W_8{}^{VI}Co@Cu_{x-1}{}^{I}Cu_{y+1}{}^{II}\text{–}BTC]$,

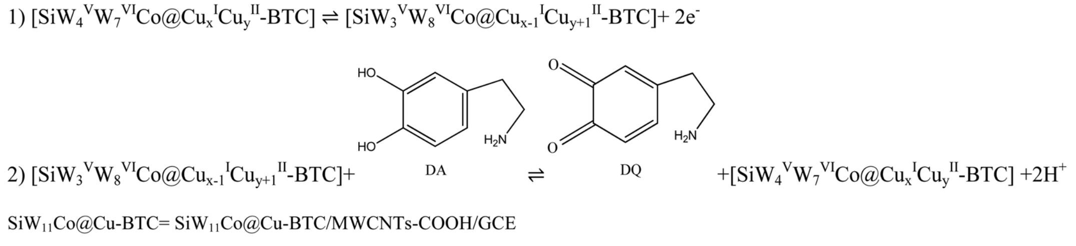
1) $[SiW_4{}^{V}W_7{}^{VI}Co@Cu_x{}^{I}Cu_y{}^{II}\text{-}BTC] \rightleftharpoons [SiW_3{}^{V}W_8{}^{VI}Co@Cu_{x-1}{}^{I}Cu_{y+1}{}^{II}\text{-}BTC] + 2e^-$

2) $[SiW_3{}^{V}W_8{}^{VI}Co@Cu_{x-1}{}^{I}Cu_{y+1}{}^{II}\text{-}BTC] +$ DA $\rightleftharpoons$ DQ $+ [SiW_4{}^{V}W_7{}^{VI}Co@Cu_x{}^{I}Cu_y{}^{II}\text{-}BTC] + 2H^+$

$SiW_{11}Co$@Cu-BTC= $SiW_{11}Co$@Cu-BTC/MWCNTs-COOH/GCE

Scheme 2 Electro-oxidation mechanism of DA at the $SiW_{11}Co$@Cu–BTC/MWCNTs-COOH/GCE.

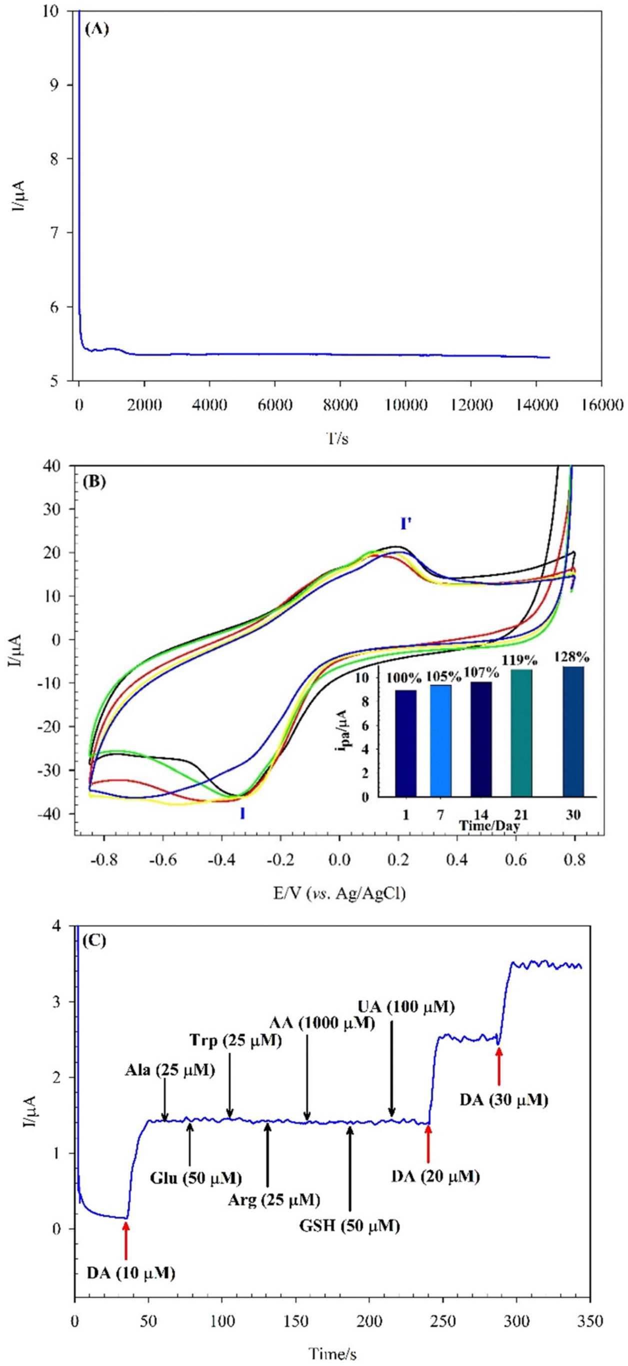

Fig. 8 (A) Stability of $SiW_{11}Co@Cu–BTC/MWCNTs-COOH/GCE$ in 0.04 M BRB (pH 7) containing 100 μM DA by chronoamperometry (*I*–*t*) at the fixed-potential of +0.25 V, (B) long-term stability of $SiW_{11}Co@Cu–BTC/MWCNTs-COOH/GCE$ in 0.04 M BRB (pH 7) during 30 days, and (C) effect of interfering species on the detection of DA at a potential of +0.25 V at $SiW_{11}Co@Cu–BTC/MWCNTs-COOH/GCE$ in 0.04 M BRB (pH 7).

which subsequently facilitates the oxidation of DA to dopamine-quinone (DQ).

3.6. Repeatability, reproducibility, and stability studies

The repeatability, reproducibility, and stability of the modified GCE were investigated under the optimal conditions.

Table 4 Results of the recovery analysis of DA spiked in real samples (*n* = 3)

Sample	Originally (μM)	Added (μM)	Found (μM)	Recovery (%)	RSD (%)
Dopadic	55	0	55.23	100.42	2.51
		50	106.26	101.20	3.24
		100	156.13	100.73	4.22
		200	254.21	99.69	3.65
Human blood serum[a]	—	0	ND[b]	—	—
		10	10.13	101.30	2.67
		20	20.57	102.85	2.49
		40	40.85	102.12	3.61

[a] Human blood serum (female, 32 years old). [b] Not detected.

Repeatability and reproducibility are vital indicators of the quality of experiments and analyses. To evaluate the repeatability of the sensor, six different CVs with one modified GCE were performed in 0.04 M BRB (pH 7) containing 0.5 mM DA. The reproducibility has been studied by six modified GCEs under similar conditions. The obtained results are given in the ESI† (Fig. S5-A and B, ESI†). The relative standard deviation (RSD) of the obtained voltammetry peak current for the repeatability and reproducibility were 3.61% and 4.39%, respectively, indicating that the prepared sensor has excellent precision.

Developing stable sensors and biosensors is one of the most essential objectives of analytical chemists. The modified electrodes based on POMs are generally known for their instability in aqueous media, which can lead to detachment from the electrode surface and subsequent dissolution in the electrolyte. Consequently, the stability of the $SiW_{11}Co@Cu–BTC/MWCNTs-COOH/GCE$ is a critical factor for the assessment to ensure reliable electrochemical performance.

Fig. 8A shows the stability of the sensor by the amperometry method in 0.04 M BRB (pH 7) containing 100 μM DA. Moreover, in Fig. 8B the long-term stability of the sensor was displayed in air at ambient temperature (25 ± 2 °C) over a period of 30 days. The peak I′ current of the $SiW_{11}Co@Cu–BTC/MWCNTs-COOH/GCE$ shows a progressive increase, a 5% increase after 7 days, followed by a 7% increase after 14 days, a 19% increase after 21 days, and a final 28% increase after one month. These results confirmed that the $SiW_{11}Co@Cu–BTC/MWCNTs-COOH/GCE$ has excellent stability that can be credited to the encapsulation of the $SiW_{11}Co$ on Cu–BTC framework and also immobilization of the $SiW_{11}Co@Cu–BTC$ compound on the MWCNTs-COOH surface, which contributes to stabilizing POMs in aqueous media and improves the electrochemical performance of the modified GCE.

3.7. Interference study

Selectivity is a crucial attribute for sensors, as it denotes the sensor's ability to distinguish the target analyte from other species in a complex mixture. The chronoamperometry method was employed to investigate the potential effects of interfering species on the detection of 10 μM DA by injecting these substances into a 0.04 M BRB (pH 7) at an optimum potential of +0.25 V. As displayed in Fig. 8C, no significant changes in current are observed for each addition of ascorbic acid (AA) at

100-fold, uric acid (UA) at 10-fold, glucose (Glu) and glutathione (GSH) at 5-fold, and alanine (Ala), arginine (Arg) and tryptophan (Trp) at 2.5-fold concentrations of DA. However, a noteworthy increase in the current was recorded with more injection of DA (20 and 30 μM), which shows the excellent selectivity of the proposed sensor. The $SiW_{11}Co$@Cu–BTC/MWCNTs-COOH/GCE exhibits superior selectivity in the oxidation of DA due to the unique structural features of the modifier and the optimization of the operating conditions, such as pH level and oxidation potential.

3.8. Analytical application

The analytical applicability of the $SiW_{11}Co$@Cu–BTC/MWCNTs-COOH/GCE was evaluated through the detection of different concentrations of DA in a dopadic ampoule, and human blood serum samples. The preparation of the dopadic sample involved the injection of 2 μL of this sample into 10 mL of a 0.04 M BRB solution (pH 7.0). In the following, the prepared solution was transferred directly into the electrochemical cell without any pretreatment procedures. For the preparation of the blood serum sample, first for deproteinization of serum, 0.5 mL $HClO_4$ (2 M) was added to 1.0 mL of the sample and stirred for 1 minute.[77] In the next step, the prepared sample was centrifuged at 1500 rpm for 10 minutes, and then diluted 20-times with 0.04 M BRB (pH 7.0) and transferred into the electrochemical cell.

Then the prepared samples (dopadic and human blood serum) were used for analysis of dopamine by SWV at the applied potential of −0.4 to +0.8 V using the standard addition method. The obtained data from the experiments are listed in Table 4. The recovery values approach near 100% with RSD less than 5% showing that this sensor is suitable for DA detection in biological fluids and the precise control of DA concentration in drugs.

4. Conclusions

A novel sensor based on a tri-component nanocomposite ($SiW_{11}Co$@Cu–BTC/MWCNTs-COOH/GCE) was designed, characterized, and employed as an efficient catalyst for the electrooxidation of DA. The sensor offers several key advantages, including rapid and simple fabrication, low LOD, a wide linear range, outstanding stability, and excellent repeatability, reproducibility, and selectivity. These superior properties are attributed to the enhanced electroactive surface area of the $SiW_{11}Co$@Cu–BTC/MWCNTs-COOH/GCE (92.65 cm^2), resulting from the synergistic effect of $SiW_{11}Co$, Cu–BTC, and MWCNTs-COOH, combined with its porous structure. Furthermore, this sensor can be effectively used for precise DA measurement in biological fluids and pharmaceutical samples, making it highly suitable for high-performance DA detection.

Data availability

All relevant data presented in this article is present in the form of figures and tables in the manuscript.

Conflicts of interest

There are no conflicts to declare.

Acknowledgements

The authors gratefully acknowledge the financial support of the Research Council of the University of Hormozgan.

References

1 L. Wang, T. Meng, J. Sun, S. Wu, M. Zhang, H. Wang and Y. Zhang, *Anal. Chim. Acta*, 2019, **1047**, 28–35.

2 J. Sun, S. Abednatanzi, P. Van Der Voort, Y.-Y. Liu and K. Leus, *Catalysts*, 2020, **10**, 578.

3 M. Samaniyan, M. Mirzaei, R. Khajavian, H. Eshtiagh-Hosseini and C. Streb, *ACS Catal.*, 2019, **9**, 10174–10191.

4 E. Rtibi, M. Abderrabba, S. Ayadi and B. Champagne, *Inorg. Chem.*, 2019, **58**, 11210–11219.

5 J. M. Clemente-Juan, E. Coronado and A. Gaita-Ariño, *Chem. Soc. Rev.*, 2012, **41**, 7464–7478.

6 S. Dianat, A.-K. Bordbar, S. Tangestaninejad, B. Yadollahi, R. Amiri, S.-H. Zarkesh-Esfahani and P. Habibi, *J. Inorg. Biochem.*, 2015, **152**, 74–81.

7 S. Dianat, A. Bordbar, S. Tangestaninejad, S. Zarkesh-Esfahani, P. Habibi and A. A. Kajani, *J. Iran. Chem. Soc.*, 2016, **13**, 1895–1904.

8 Y. Zhang, J. Liu, S.-L. Li, Z.-M. Su and Y.-Q. Lan, *EnergyChem*, 2019, **1**, 100021.

9 B. Lu, S. Li, J. Pan, L. Zhang, J. Xin, Y. Chen and X. Tan, *Inorg. Chem.*, 2020, **59**, 1702–1714.

10 F. Duan, X. Liu, D. Qu, B. Li and L. Wu, *CCS Chem.*, 2021, **3**, 2676–2687.

11 X. Yang, C. Zhu, L. Zeng, W. Xue, L. Zhang, L. Zhang, K. Zhao, M. Lyu, L. Wang and Y.-Z. Zhang, *Chem. Sci.*, 2022, **13**, 5920–5928.

12 A. Karimi-Takallo, S. Dianat and A. Hatefi-Mehrjardi, *J. Electroanal. Chem.*, 2021, **886**, 115139.

13 M. Sharifi, S. Dianat and A. Hosseinian, *RSC Adv.*, 2021, **11**, 8993–9007.

14 S.-H. Ge, L.-P. Cui, K. Yu, M.-L. Wang, C.-M. Wang, L.-X. Guo and B.-B. Zhou, *Tungsten*, 2023, **5**, 270–276.

15 H. Ravanbakhsh and S. Dianat, *Sens. Bio-Sens. Res.*, 2023, **40**, 100556.

16 F. Boussema, R. Haddad, Y. Ghandour, M. S. Belkhiria, M. Holzinger, A. Maaref and S. Cosnier, *Electrochim. Acta*, 2016, **222**, 402–408.

17 Q. Wang, J. Khungwa, L. Li, Y. Liu, X. Wang and S. Wang, *J. Electroanal. Chem.*, 2018, **824**, 91–98.

18 H. Ravanbakhsh, S. Dianat and A. Hosseinian, *RSC Adv.*, 2022, **12**, 9210–9222.

19 R. Hashemniaye-Torshizi, N. Ashraf, M. H. Arbab-Zavar and S. Dianat, *Catal. Sci. Technol.*, 2021, **11**, 1098–1109.

20 P. Shestakova, M. Popova, A. Szegedi, H. Lazarova, T. K. N. Luong, I. Trendafilova, J. Mihaly and T. N. Parac-Vogt, *Microporous Mesoporous Mater.*, 2021, **323**, 111203.

21 J. Selvam, B. Samannan, P. Peter and J. Thavasikani, *Polym. Polym. Compos.*, 2021, **29**, 373–382.

22 S. Li, X. Tan, M. Yue, L. Zhang, D. Chai, W. Wang, H. Pan, L. Fan and C. Zhao, *Chem. Commun.*, 2020, **56**, 15177–15180.

23 J. Annamalai, P. Murugan, D. Ganapathy, D. Nallaswamy, R. Atchudan, S. Arya, A. Khosla, S. Barathi and A. K. Sundramoorthy, *Chemosphere*, 2022, **298**, 134184.

24 M. Bonneau, C. Lavenn, P. Ginet, K.-i Otake and S. Kitagawa, *Green Chem.*, 2020, **22**, 718–724.

25 M. X. Wu and Y. W. Yang, *Adv. Mater.*, 2017, **29**, 1606134.

26 J. Cao, X. Li and H. Tian, *Curr. Med. Chem.*, 2020, **27**, 5949–5969.

27 Y. Y. Cai, Q. Yang, Z. Y. Zhu, Q. H. Sun, A. M. Zhu, Q. G. Zhang and Q. L. Liu, *J. Membr. Sci.*, 2019, **590**, 117277.

28 Z.-Q. Shi, N.-N. Ji, M.-H. Wang and G. Li, *Inorg. Chem.*, 2020, **59**, 4781–4789.

29 E. D. Spoerke, L. J. Small, M. E. Foster, J. Wheeler, A. M. Ullman, V. Stavila, M. Rodriguez and M. D. Allendorf, *J. Phys. Chem. C*, 2017, **121**, 4816–4824.

30 J. Dou, C. Zhu, H. Wang, Y. Han, S. Ma, X. Niu, N. Li, C. Shi, Z. Qiu and H. Zhou, *Adv. Mater.*, 2021, 2102947.

31 S. Gao, Y. Sui, F. Wei, J. Qi, Q. Meng and Y. He, *J. Mater. Sci.*, 2018, **53**, 6807–6818.

32 Y. Wang, Y. Liu, H. Wang, W. Liu, Y. Li, J. Zhang, H. Hou and J. Yang, *ACS Appl. Energy Mater.*, 2019, **2**, 2063–2071.

33 D. Wang, D. Jana and Y. Zhao, *Acc. Chem. Res.*, 2020, **53**, 1389–1400.

34 A. Bieniek, A. P. Terzyk, M. Wiśniewski, K. Roszek, P. Kowalczyk, L. Sarkisov, S. Keskin and K. Kaneko, *Prog. Mater. Sci.*, 2021, **117**, 100743.

35 K. Shen, X. Chen, J. Chen and Y. Li, *ACS Catal.*, 2016, **6**, 5887–5903.

36 H. T. Nguyen, D. N. Doan and T. Truong, *J. Mol. Catal. A: Chem.*, 2017, **426**, 141–149.

37 Q. Wang and D. Astruc, *Chem. Rev.*, 2019, **120**, 1438–1511.

38 K. N. Chappanda, O. Shekhah, O. Yassine, S. P. Patole, M. Eddaoudi and K. N. Salama, *Sens. Actuators, B*, 2018, **257**, 609–619.

39 L. Wang, Z. Hu, S. Wu, J. Pan, X. Xu and X. Niu, *Anal. Chim. Acta*, 2020, **1121**, 26–34.

40 L. Chen and Q. Xu, *Matter*, 2019, **1**, 57–89.

41 L.-J. Xu, C.-M. Wang, K. Yu, C.-X. Wang and B.-B. Zhou, *Coord. Chem. Rev.*, 2023, **481**, 215044.

42 S. N. Nobar, *Mater. Chem. Phys.*, 2018, **213**, 343–351.

43 S. S.-Y. Chui, S. M.-F. Lo, J. P. Charmant, A. G. Orpen and I. D. Williams, *Science*, 1999, **283**, 1148–1150.

44 Y. Song, M. Xu, C. Gong, Y. Shen, L. Wang, Y. Xie and L. Wang, *Sens. Actuators, B*, 2018, **257**, 792–799.

45 M. Saraf, R. Rajak and S. M. Mobin, *J. Mater. Chem. A*, 2016, **4**, 16432–16445.

46 T. Shen, T. Liu, H. Mo, Z. Yuan, F. Cui, Y. Jin and X. Chen, *RSC Adv.*, 2020, **10**, 22881–22890.

47 Z. Meng, M. Li, X. Liu and Z. Lei, *J. Mater. Sci.: Mater. Electron.*, 2019, **30**, 18617–18625.

48 W. Meng, S. Xu, L. Dai, Y. Li, J. Zhu and L. Wang, *Electrochim. Acta*, 2017, **230**, 324–332.

49 M. Hosseini, S. Zeinali and M. Sheikhi, *Sens. Actuators, B*, 2016, **230**, 9–16.

50 L. Ji, J. Hao, K. Wu and N. Yang, *J. Phys. Chem. C*, 2019, **123**, 2248–2255.

51 L. Ji, Q. Cheng, K. Wu and X. Yang, *Sens. Actuators, B*, 2016, **231**, 12–17.

52 Y. Cao, L. Wang, C. Shen, C. Wang, X. Hu and G. Wang, *Sens. Actuators, B*, 2019, **283**, 487–494.

53 C. Wang, M. Zhou, Y. Ma, H. Tan, Y. Wang and Y. Li, *Chem. – Asian J.*, 2018, **13**, 2054–2059.

54 Y. Zhang, Y. Zhang, L. Li, J. Chen, P. Li and W. Huang, *J. Electroanal. Chem.*, 2020, **861**, 113939.

55 L. Yu, K. Ning, W. Chunmei, Y. Kai, L. Jinghua, W. Chunxiao and Z. Baibin, *Dalton Trans.*, 2022, **51**, 7613–7621.

56 L. Xu, X. Zhao, K. Yu, C. Wang, J. Lv, C. Wang and B. Zhou, *CrystEngComm*, 2022, **24**, 5614–5621.

57 D. Rudakiya, Y. Patel, U. Chhaya and A. Gupte, *Nanotechnology for Agriculture: Advances for Sustainable Agriculture*, 2019, pp. 121–130.

58 X. Kong, Y. Wang, Q. Zhang, T. Zhang, Q. Teng, L. Wang, H. Wang and Y. Zhang, *J. Colloid Interface Sci.*, 2017, **505**, 615–621.

59 J. Jiao, J. Zuo, H. Pang, L. Tan, T. Chen and H. Ma, *J. Electroanal. Chem.*, 2018, **827**, 103–111.

60 T. J. Weakley and S. Malik, *J. Inorg. Nucl. Chem.*, 1967, **29**, 2935–2944.

61 T. Wei, M. Zhang, P. Wu, Y.-J. Tang, S.-L. Li, F.-C. Shen, X.-L. Wang, X.-P. Zhou and Y.-Q. Lan, *Nano Energy*, 2017, **34**, 205–214.

62 M. Vepsäläinen, M. Chen, Y. Yang, R. Brokenshire and T. Muster, *J. Appl. Electrochem.*, 2014, **44**, 1135–1143.

63 H. S. Magar, R. Y. Hassan and A. Mulchandani, *Sensors*, 2021, **21**, 6578.

64 Z. Liu, M. Jin, J. Cao, J. Wang, X. Wang, G. Zhou, A. van den Berg and L. Shui, *Sens. Actuators, B*, 2018, **257**, 1065–1075.

65 D. Zhu, H. Ma, Q. Zhen, J. Xin, L. Tan, C. Zhang, X. Wang and B. Xiao, *Appl. Surf. Sci.*, 2020, **526**, 146721.

66 S. Ramakrishnan, K. Pradeep, A. Raghul, R. Senthilkumar, M. Rangarajan and N. K. Kothurkar, *Anal. Methods*, 2015, **7**, 779–786.

67 S. Wang, W. Zhang, X. Zhong, Y. Chai and R. Yuan, *Anal. Methods*, 2015, **7**, 1471–1477.

68 Y.-S. Hsieh, B.-D. Hong and C.-L. Lee, *Microchim. Acta*, 2016, **183**, 905–910.

69 R. Nehru and S. M. Chen, *RSC Adv.*, 2018, **8**, 27775–27785.

70 S. Rong, P. Zhang, L. Zou, Y. Tian, M. Miao, D. Jia, R. Qiu, F. Qi, H. Ma and H. Pan, *IEEE Sens. J.*, 2022, **22**, 5540–5547.

71 C. Luhana and P. Mashazi, *Electrocatalysis*, 2022, **14**, 406–417.

72 X. Wang, Y. Zhao, D. Zhang, S. Rong and H. Ma, *Int. J. Electrochem. Sci.*, 2019, **14**, 3595–3609.

73 J. Li, J. Xia, F. Zhang, Z. Wang and Q. Liu, *J. Chin. Chem. Soc.*, 2018, **65**, 743–749.

74 B. Ma, H. Guo, M. Wang, L. Li, X. Jia, H. Chen, R. Xue and W. Yang, *Electroanalysis*, 2019, **31**, 1002–1008.

75 K. Liu, Y. Chen, X. Dong and H. Huang, *Inorg. Chem. Commun.*, 2022, **142**, 109584.

76 S. Ahmadi Direstani and S. Dianat, *Mater. Adv.*, 2023, **4**, 5761–5774.

77 R. Karimi Shervedani, S. Bahrani, M. Samiei Foroushani and F. Momenbeik, *Electroanalysis*, 2017, **29**, 272–279.